HHS Public Access

Author manuscript

Med Phys. Author manuscript; available in PMC 2022 May 01.

Published in final edited form as:

Med Phys. 2021 May ; 48(5): 2553–2565. doi:10.1002/mp.14816.

In-vivo evaluation of angulated needle-guide template for MRI-guided transperineal prostate biopsy

Pedro Moreira[1,*], **John Grimble**[2,*], **Nicusor Iftimia**[2], **Camden P Bay**[1], **Kemal Tuncali**[1], **Jesung Park**[2,†], **Junichi Tokuda**[1,†,#]

[1]Department of Radiology, Brigham and Women's Hospital and Harvard Medical School, 75 Francis St., Boston MA, USA

[2]Physical Sciences Inc., 20 New England Bus Center Dr, Andover MA, USA.

Abstract

Purpose: Magnetic Resonance Imaging (MRI)-guided transperineal prostate biopsy has been practiced since the early 2000s. The technique often suffers from targeting error due to deviation of the needle as a result of physical interaction between the needle and inhomogeneous tissues. Existing needle guide devices, such as a grid template, do not allow choosing an alternative insertion path to mitigate the deviation because of their limited degree-of-freedom (DoF). This study evaluates how an angulated needle insertion path can reduce needle deviation and improve needle placement accuracy.

Methods: We extended a robotic needle-guidance device (Smart Template) for in-bore MRI-guided transperineal prostate biopsy. The new Smart Template has a 4-DoF needle guiding mechanism allowing a translational range of motion of 65 mm and 58 mm along the vertical and horizontal axis, and a needle rotational motion around the vertical and horizontal axis $\pm 30°$ and a vertical rotational range of $[-30°, +10°]$, respectively. We defined a path planning strategy, which chooses between straight and angulated insertion paths depending on the anatomical structures on the potential insertion path. We performed 1) a set of experiments to evaluate the device positioning accuracy outside the MR-bore, and 2) an *in vivo* experiment to evaluate the improvement of targeting accuracy combining straight and angulated insertions in animal models (swine, $n = 3$).

Results: We analyzed 46 *in vivo* insertions using either straight or angulated insertions paths. The experiment showed that the proposed strategy of selecting straight or angulated insertions based on the subject's anatomy outperformed the conventional approach of just straight insertions in terms of targeting accuracy (2.4 mm [1.3–3.7] vs. 3.9 mm [2.4–5.0] {Median [IQR]}); $p =$ 0.041 after the bias correction).

Conclusion: The *in vivo* experiment successfully demonstrated that an angulated needle insertion path could improve needle placement accuracy with a path planning strategy that takes account of the subject-specific anatomical structures.

[#]Corresponding author: Junichi Tokuda, 75 Francis Street, Department of Radiology, Brigham and Women's Hospital, ASB-I, Room L1-050, Boston, MA 02115, USA, tokuda@bwh.harvard.edu.

[*]Both authors contributed equally to this work

[†]Senior authors, equal contribution

I. INTRODUCTION

Prostate cancer is one of the most common types of cancer among men in the United States, with more than 174,000 estimated new cases annually.[1] Prostate cancer is commonly diagnosed with systematic biopsies, where tissues are sampled from 6 to 12 locations in the prostate under transrectal ultrasound (TRUS)-guidance. While TRUS-guided biopsies have been widely adopted thanks to its ease-of-use, its inability to target suspicious lesions raised a concern of false-negative biopsies. Alternatively, Magnetic Resonance Imaging (MRI) has been used to guide prostate biopsies,[2–4] allowing physicians to sample tissues specifically from suspected lesions known as targeted biopsies. MRI-targeted biopsies can be achieved by either superimposing preprocedural MRI over the intraprocedural TRUS images (MR-TRUS fusion biopsy) or performing a biopsy in the MRI scanner (in-bore MRI-guided biopsy). While MRI-targeted biopsies are not as common as conventional TRUS-guided systematic biopsies, a recent multi-center study has shown that a diagnostic pathway involving MRI-targeted biopsies outperformed the conventional pathway with TRUS-guided systematic biopsies in terms of both overall clinical outcomes and health economics perspective.[5]

The common technical challenge for targeted biopsies is to accurately place a biopsy needle into the suspected lesion found on MRI regardless of the approach (i.e., MR-TRUS fusion biopsy or in-bore MRI-guided biopsy). A simulation study demonstrated that the misplacement of a needle could significantly affect the diagnostic sensitivity and specificity; [6] the sensitivity for cancer detection using a 3-core approach dropped from 0.86 to 0.62 when the targeting error increased from 1 mm to 5 mm. Although repeated needle insertions may compensate for inaccurate needle placement, it would lead to increased procedure time, patient discomfort, and excessive injury to the patient. To achieve accurate needle placement, a needle-guiding device is often used to direct the biopsy needle to the lesion mechanically, such as a grid template. Researchers have also been developing and testing computer-controlled needle-guiding manipulators for transrectal,[7–9] transperineal,[10–13] and transgluteal[14] needle placements. Zangos et al. presented one of the first studies with a computer-controlled guiding device for MRI-guided biopsies in clinical trials.[15] The study used a pneumatic-actuated robotic system to improve needle placement accuracy and reduce the procedure time in transgluteal biopsies. Schouten et al. introduced a pneumatic-actuated device for transrectal prostate biopsies tested in 13 patients, which achieved a 5.7 mm average targeting error.[8] Stoianovici et al. presented an MR-safe device for transrectal biopsies using pneumatic stepper motors, which was tested in 5 patients with a targeting accuracy of 2.58 mm.[16] Our team has also performed studies using robotic devices for MRI-guided prostate biopsies in clinical trials. Tilak et al. reported a study analyzing the clinical outcomes of MRI-guided transperineal prostate biopsies with and without the assistance of a robotic device.[17] Although the mean targeting error was not significantly different (5.42 mm vs 6.05 mm), an improvement on the mean accuracy of the best needle placement were observed using the robotic device (2.39 mm vs 3.71 mm). The best attempt was usually achieved after multiple needle insertion attempts and image-based assessment of needle placement accuracy. While the current gold standard in MRI-guided targeted biopsies is to perform multiple insertions until the desired accuracy is achieved, the excessive number of

insertions may increase tissue damage, patient discomfort and increase the procedure time. Therefore, reducing the number of insertion attempts while maintaining the same accuracy level is essential to improve the overall clinical outcomes of transperineal prostate biopsies.

Recently, Moreira et al. reported another study analyzing needle insertion trajectories during robot-assisted MRI-guided transperineal prostate biopsies.[18] The analysis revealed that extra-prostatic tissues could influence the accuracy of the needle placement. The results showed that insertions crossing specific anatomic structures, such as the bulbospongiosus, resulted in a reduced targeting error, suggesting that a patient-specific path planning strategy considering the target location and the extra-prostatic tissues may improve the targeting accuracy of transperineal biopsy. However, such a method requires specific kinematics approaches of the guiding device and has not been well explored. Although a few studies presented robots that are able to perform angulated insertions,[16,13] their primary goal of the angulated insertions is to either achieve the sufficient range of motion of the device in the limited space,[16] or to avoid artificial obstacles placed on a phantom.[13] None of these studies explored the idea of using angulated insertions to select an insertion path based on the patient anatomy.

In this study, we present a four degree-of-freedom (DoF) needle-guide manipulator named Smart Template that allows angulating the needle insertion path to a given target. The Smart Template is extended from a 2-DoF motorized template,[19] which was previously tested in 43 patients.[17,20] While the previous device had 2 DoF for translational motions along the right-left axis and the anterior-posterior axis, the current system has 2 extra DoF for the angulations around the right-left axis and the anterior-posterior axis. The device was designed for in-bore MR-guided interventions and the use of TRUS imaging for guidance is not considered in the current version of the system. We hypothesize that the additional DoF will allow selecting an alternative path based on subject-specific anatomical structures to mitigate severe needle deviation, which will improve needle placement accuracy. We performed laboratory experiments to evaluate the device targeting accuracies, and an *in vivo* experiment to evaluate the improvement of targeting accuracy with the proposed angulation strategy in animal models.

II. METHODS

A. Mechanical design of Smart Template

The design of the Smart Template is shown in Figure 1. In our design, we considered the fact that the device has to enable the use of an 18-gauge core biopsy needle, which will be placed within a needle guide oriented toward a target lesion identified on an MR image, while a physician has to manually insert the needle. The Smart Template dimensions are 217 mm (H) x 451 mm (L) x 142 (W) mm (Figure 1.a). The entry point on the skin can be selected by translating the needle guide in the horizontal (R-) and vertical (A-) directions, which corresponds to the right-left and anterior-posterior directions in the patient coordinate system (Figure 1.b). The needle guide can be angulated horizontally and vertically, to change the orientation of the needle insertion path (Figures 1.c–d).

The needle guide is driven by a set of stages consisting of two translational stages and two angulation stages. Each translational stage is mechanically coupled to an ultrasonic motor (USR60-E3N, Shinsei Corp., Tokyo, Japan) via a set of brass lead screws (1/4–20 ACME) that convert the rotational motion into linear translation. The lead screws are connected via a timing belt (MXL-type, 1/8-inch width, 0.08-in pitch, urethane body, with a Kevlar core) to ensure synchronous movement. The stages used for needle angulation are driven by a set of non-magnetic piezoelectric motors (Piezo LEGS LS1510D-B15, PiezoMotor Corp., Uppsala, Sweden) with a positioning resolution of < 1 nm, which is equivalent of the theoretical tilting step of 10^{-5} degrees. Optical encoders (ATOM4T1–080, Renishaw, Gloucestershire, UK) and glass scales are attached to the piezoelectric motor and the translating stage, respectively to determine the current positions of the angulation stages with < 0.1° resolution. The needle guide is held at the centers of the two angulation stages via plastic spherical bearings. The relative position between these spherical bearings defines the orientation of the needle guide. The angulation stages are decoupled from the global translation so that the translation and angulation of the needle can be controlled independently.

The device is placed on a custom-made patient table with sliding rails, which allows adjusting the device against the patient perineum to minimize the air gap between the device guide and the skin surface (Figure 2). Additionally, the needle guide can be extended to eliminate the air gap and avoid the out-of-tissue needle deflection during the perineum puncture. During the procedure, the clinician extends the needle guide until soft contact is made with the patient skin, and only then the needle is inserted. The needle guide can be detached for sterilization and is used to avoid direct contact of the device with the needle.

An acrylic cube with a set of seven cylindrical MR-visible markers (MR-SPOT 121, Beekley Medical, Bristol, CT) called “zFrame” is attached to the Smart Template (Figure 2). The markers are scanned at the beginning of the procedure to register the device coordinate system to the MRI coordinate system. After the registration is performed, the zFrame is removed. The configuration of the z-frame allows software to automatically detect and localize the cube on a single- or multi-slice MR image[21] and co-register the MRI and Smart Template coordinate systems.

B. Controller

The motors and the encoders are connected to a robotic controller located in the MR control room. The controller drives the motors to align the needle guide towards the defined target location. Low-level positioning control of each motor is achieved by a motion controller (DMC-4183, Galil Motion Control, Rocklin, CA), which can control up to eight motors. The motion controller is connected to two ultrasonic motor drivers (D6060E, Shinsei Corp., Tokyo, Japan) and two piezoelectric motor drivers (PMCM31–01, PiezoMotor Uppsala AB, Uppsala, Sweden) to control individual motors for translation and angulation of the needle guide. For safety reasons, the ultrasonic and piezoelectric drivers are only powered when an MRI-compatible pneumatic footswitch (6210-OB, Herga Technology Ltd, Suffolk, UK) is activated by the clinician standing in front of the gantry. This ensures that the device only moves under the clinician’s direct supervision. The controller also houses a low-power

single-board computer (SBC) with a system-on-chip (Sitara AM335x ARM Cortex-A8, Texas Instruments, Dallas, TX) and a Linux OS to handle communication between the motion controller and a user interface (see the next section and Figure 3). The SBC runs a Robot Operating System (ROS), which receives commands from the user interface (i.e., template location, target location, desired angulation), and calculates the desired position of each motor. The SBC communicates with the user interface over Ethernet using the OpenIGTLink protocol[22] and ROS-IGTL-Bridge.[23]

Once the user defines the location of the target on the MR images ($\boldsymbol{p}_t^i$) and set the desired insertion angles [$\alpha\ \beta$] on the user interface, these parameters are transferred to the SBC via OpenIGTLink. The Python script then calculates the target location with respect to the Smart Template base location ($\boldsymbol{p}_t^b$), such as:

$$\boldsymbol{p}_t^b = \left(\boldsymbol{T}_z^i \boldsymbol{T}_b^z\right)^{-1} \boldsymbol{p}_t^i \tag{1}$$

where $\boldsymbol{T}_z^i$ is the homogeneous transformation between the image reference frame and the z-frame[21], $\boldsymbol{T}_b^z$ is the rigid transformation between the z-frame location and the Smart Template homing position (base) and $\boldsymbol{p}_t^b = \left[q_R\ q_A\ q_S\ 1\right]^t$ (Figure 4). The robot's inverse kinematic equations are used to determine the desired position of the translational stages actuated by the ultrasonic motors ($\boldsymbol{p}_{us}$) and the angulation stages actuated by the piezoelectric ($\boldsymbol{p}_{pe}$) motors, such that

$$\boldsymbol{p}_{pe} = \begin{bmatrix} p_R \\ p_A \end{bmatrix} = d_1 \begin{bmatrix} \tan\alpha \\ \tan\beta \end{bmatrix} \tag{2}$$

where p_R and p_A are the desired positions for the angulation stages along the axis R and A, α and β are the desired insertion angles, and d_1 is the distance between the two spherical joints (Figure 4). The position of the translation stages (u_R and u_A) is then given by

$$\boldsymbol{p}_{US} = \begin{bmatrix} u_R \\ u_A \end{bmatrix} = \begin{bmatrix} q_R - p_R + q_S \tan\alpha \\ q_A + q_S \tan\beta \end{bmatrix}. \tag{3}$$

If the values of $\boldsymbol{p}_{pe}$ and $\boldsymbol{p}_{US}$ are outside the Smart Template's motion range, the SBC informs the user that the selected path is unfeasible and waits for a new set of target locations and desired insertion angles. If the path is considered feasible, the desired positions of the ultrasonic and piezoelectric motors are then transmitted to the motion controller, which runs independent PID controllers for each motor separately.

C. User interface

The user interface was implemented based on 3D Slicer, an open-source software platform for medical image informatics, processing, and visualization.[24] It provides an interactive graphical environment for the user to 1) review pre- and intra-procedural MRI, 2) define target points and needle insertion paths on the images, 3) send commands to the robot

controller, and 4) confirm the needle placement with intra-procedural MRI acquired after the insertion. The user interface communicates with the robot controller using OpenIGTLink,[22] a network communication interface for image-guided interventions.

D. Experiments

We performed two sets of experiments to evaluate the functionality of the Smart Template and its ability to improve targeting accuracy in transperineal prostate biopsy with angulated needle insertion. First, we tested the device in a benchtop experimental setup to assess the movement accuracy. Next, we performed an *in vivo* experiment to evaluate the improvement of targeting accuracy in animal models using a strategy to angulate the insertions and mitigate the needle deviation. Our strategy is to employ an alternative insertion path when the needle is likely to deviate. Based on our clinical observations where the needle was inserted into the prostate transperineally along the body axis of the patient, the needle tends to deviate laterally (i.e. away from the midline) when it is inserted into the target in the lateral side of the prostate. While this observation is anecdotal, the finding is consistent with our previous study on the analysis of needle insertion trajectories.[18] The study found that the trajectories that crossed the bulbospongiosus resulted in a smaller targeting error likely due to the absence of the pelvic diaphragm on those trajectories (Figure 5). Therefore, we hypothesized that the needle placement error could be reduced by inserting the needle through the bulbospongiosus. Such an insertion trajectory can be achieved by angulating the needle when the target is not behind the bulbospongiosus from the needle guide (Figure 6). Hence, our *proposed path selection strategy* considers straight insertion when the target is located behind the bulbospongiosus and angulated insertions crossing the bulbospongiosus otherwise. In designing the *in vivo* experimental protocol to determine whether the aforementioned strategy is effective, we consider the following research questions:

1. Does the path selection strategy result in a higher targeting accuracy than the conventional approach where the needle is always inserted without angulation (straight-only) and an approach where the needle is always angulated (angulation-only)?
2. Does the angulation strategy result in a higher targeting accuracy than repeated needle insertions using the same path?

To answer those questions, we performed *in vivo* experiments in three animal models inserting an MRI compatible biopsy needle into the pelvic region of the models. Before the *in vivo* experiments, an accuracy test of the Smart Template was conducted outside the MRI environment.

D.1 Smart Template evaluation

D.1.1 Needle guide movement accuracy: We assessed the positioning and angulation accuracies of the Smart Template in a laboratory setting using an optical tracker. The Smart Template was programmed to position the needle at 15 different target locations, ranging from −17 mm to 14 mm along the horizontal axis and from −19 mm to 15 mm along the vertical axis. We also defined 15 different orientations with α varying from -15° to 22° and β varying from -15° to 10°. As the translation and angulation movements are independent of

each other, we tested them separately. The resultant position and orientation of the needle were measured using a 6-DoF optical tracker (Polaris Vicra, Northern Digital Inc., Waterloo, Ontario, Canada) as a reference, which has an accuracy of 0.25 mm with a 95% Confidence Interval of 0.5 mm. The passive markers (Rigid Body 1, Northern Digital Inc., Waterloo, Ontario, Canada) was placed directly on the back of the needle guide. The translation and angular errors between the desired and resultant positions and orientations were evaluated.

D.1.2 Needle insertion in free-space: Needle insertions in free space were performed to assess the targeting accuracy in an ideal situation without the needle-tissue interaction. We conducted 44 planar insertions divided into three groups: 22 straight insertions, 11 insertions with vertical angulation, and 11 insertions with horizontal angulations. We used 22 randomly selected targets at an insertion depth of 100 mm and insertion angles α varying from -15° to 15° and β varying from -10° to 10°, which are within the range of insertion angles used in the animal experiment. For each target, one straight and one angulated insertion were performed. The needle tip location was defined using a camera-based tracking algorithm. The camera (PowerShot SX30, Canon Inc., Tokyo, Japan) was placed perpendicular to the insertion plane, and an image was taken after each insertion with a pixel size of 0.25 mm × 0.25 mm. The needle tip location was extracted from the post-insertion image using a sequence of image processing techniques and the Harris corner detection algorithm[25] implemented in Python. The targeting error was considered the Euclidian distance between the target location and the final needle tip position.

D.1.3 MRI-compatibility: The impact of the Smart Template on the image quality was evaluated by measuring the signal-to-noise-ratio (SNR). We evaluated the compatibility of the Smart Template in a 3-Tesla MRI scanner (MAGNETOM Skyra 3T, Siemens Healthineers, Erlangen, Germany). The SNR was computed as the mean signal in the center of a phantom for image quality purposes (Ultra-Cal Inc., Escondido, CA, USA) divided by the noise calculated according to the National Electrical Manufacturers Association (NEMA) standard MS1–2008. Mean signal was defined as the mean pixel intensity in the region of interest. The analysis was performed using two imaging protocols commonly used in MRI-guided biopsies: T2-weighted turbo spin echo (TSE) sequence (TR/TE = 4800/86 ms, flip angle = 173°, echo train length = 15, matrix = 512×512, pixel size = 0.3125×0.3125 mm, slice thickness = 3 mm, FOV= 160×160 mm) and the volume-interpolated breath-hold examination (VIBE) sequence (TR/TE = 2400/102 ms, flip angle = 128°, echo train length = 15, matrix = 256×256, pixel size = 0.70×0.70 mm, slice thickness = 2 mm, FOV= 180×180 mm). We compared the SNR values between three different configurations: 1) baseline (without the Smart Template), 2) Smart Template powered off, and 3) Smart Template powered on.

D.2 *In vivo* evaluation of straight and angulated insertions

D.2.1 Experimental protocol: The study has been reviewed and approved by the Institutional Animal Care and Use Committee (IACUC) at Brigham and Women's Hospital. We performed mock biopsy procedures in animal models (male Yorkshire, 30–40 kg, N=3) in a whole-body 3-Tesla MRI scanner (MAGNETOM Skyra 3T, Siemens Healthineers, Erlangen, Germany) to test if the additional DoF of the Smart Template can help to mitigate

the needle deviation and improve needle placement accuracy for transperineal prostate biopsy.

The procedures were performed as follows. The subject was orally intubated with a cuffed endotracheal tube after an application of the topical anesthetic. The endotracheal tube was secured to the snout with flexible rubber tubing, and the subject received between 1–3L oxygen and between 1–4% Isoflurane before being transported to the MRI scanner room. Vital signs and depth of anesthesia were continuously monitored with a combination of a pulse oximeter, end-tidal CO_2 monitor, and respiration volume/rate throughout the procedure. After the subject was placed on the patient table of the MRI scanner in the lithotomy position, the Smart Template was placed in front of the perineum (Figure 7). The subject was then moved to the isocenter where images were acquired. An axial T2-weighted MRI of the prostate (planning image) was first obtained using a turbo spin echo (TSE) sequence (TR/TE = 4800/86 ms, flip angle = 173°, echo train length = 15, matrix = 512×512, pixel size = 0.3125×0.3125 mm, slice thickness = 3 mm, FOV= 160×160 mm) to define targets in the pelvic area. An image of the Z-frame (z-frame image) was then acquired using a volume-interpolated breath-hold examination (VIBE) sequence (TR/TE = 2400/102 ms, flip angle = 128°, echo train length = 15, matrix = 256×256, pixel size = 0.70×0.70 mm, slice thickness = 2 mm, FOV= 180×180 mm). The images were transferred to the user interface software (3D Slicer), where the targets were randomly selected in the pelvic area on the planning image. The transformation between the image and the device coordinate systems were determined using the registration algorithm developed in our previous study.[21] After the insertion plan was finalized, the coordinates of the targets were transformed to the device coordinate system and transferred to the robot controller. For each target, a pair of needle insertions were performed using straight and angulated insertion trajectories. To answer the aforementioned research questions, two sets of experiments were performed.

Experiment 1: We angulated the insertion path with an angle varying between 0 and 15 degrees to cross the bulbospongiosus to address question 1. The targeting errors were pair-wise compared between (1-a) straight insertion only, (1-b) angulated insertion only, and (1-c) combined straight and angulated insertion using the proposed path selection strategy (i.e., straight insertion when the target is located behind the bulbospongiosus, and angulated insertion crossing the bulbospongiosus otherwise).

Experiment 2: We repeated needle placement for the same targets and insertion paths as Experiment 1 to address question 2. The one with the smaller error was chosen as the final result for the repeated insertion. This simulates a clinical practice where insertion is repeated to increase the chance of hitting the target.[6]

Once the needle guide was moved to the designated position, an 18-gauge core biopsy needle (MRI Bio Gun, EZ-EM, Westbury, NY) was manually inserted through the guide. After each insertion, a 3D T1-weighted MRI (confirmation image) was acquired using the VIBE sequence (TR/TE = 3.32/1.29 ms, flip angle = 9°, echo train length = 1, matrix = 256×256, pixel size = 0.9375×0.9375 mm, slice thickness = 3 mm, FOV= 240×240 mm) to confirm the needle placement. The images were stored and assessed after the procedure. The needle was manually segmented by the same user to avoid the user-dependencies inherent in

manual segmentations. The needle placement error was evaluated by measuring the minimum Euclidean distance between the center of the needle artifact and the pre-defined target on the axial slice. The offset in the superior-inferior axis (the axis perpendicular to the axial plane) was neglected because the biopsy needle collects a tissue sample of approximately 17 mm in length. In addition, most of the errors on the superior-inferior axis is a direct result of the manual adjustment of the insertion depth.

We also performed an additional experiment (**Experiment 3**) to test the feasibility of angulating the needle in the vertical direction. For this experiment, we simply performed needle placement with straight and vertically angulated needle paths, without any path selection strategy. We performed this additional experiment, because the capability to angulate vertically was not required in the previous experiments due to the anatomical configuration of the models, but it would be required in the future human study depending on the configuration.

D.2.2 Statistical analysis: Targeting errors achieved during the animal experiments are reported as means ± standard deviations for the normally distributed data and median plus the interquartile range (IQR) for the data which is not normally distributed. The targeting error of the conditions were pair-wise compared by using two-tailed paired t-tests. The normality of the targeting error distributions were tested using the Shapiro-Wilk test. When the normality test provided evidence of non-normality, a logarithmic transformation was used to normalize the data for the hypothesis test in order to accommodate statistical analysis using the paired t-test described above.[17] For all tests, a p-value less than 0.05 was considered to indicate a statistically significant difference.

III. RESULTS

A. Smart Template evaluation

A.1 Needle guide movement accuracy—The system presented a translational error of 0.95±0.67 mm (mean±SD) in the horizontal direction and 0.80±0.48 mm in the vertical direction. The angular error was 0.48°±0.34° and 0.44°±0.51° for the horizontal and vertical angulations, respectively.

A.2 Needle insertion in free-space—The average targeting error achieved in the 44 free-space insertions was 1.3±0.7 mm (mean±SD). The straight insertions resulted in a targeting error of 1.1±0.6 mm, while the angulated insertions had a targeting error of 1.5±0.8 mm.

A.3 MRI-compatibility—The device caused an expected SNR decrease with both protocols. When performing the T2-weighted imaging protocol, the SNR reduced from 494.1 (baseline) to 267.0 (device powered off), and to 76.4 (device powered). A similar reduction was observed when performing the VIBE imaging protocol: 183.7 (baseline), 130.5 (device powered off), and 41.9 (device powered).

B. In vivo evaluation of straight and angulated insertions

A total of 65 needle insertions were performed, including 33 straight insertions and 32 angulated insertions. Nineteen insertions were excluded from our analysis due to technical issues including poor visibility of the needle on the confirmation image (3 straight insertions and 1 angulated insertion); failure due to the presence of the bone (2 straight insertions and 1 angulated insertion); a bent needle due to excessive insertion force (1 angulated insertion); a worn-out timing belt due to extreme mechanical tests prior to the study (2 straight insertions and 2 angulated insertions); insertions not following the strategy (2 angulated insertions); and unpaired insertions due to the exclusions mentioned above (4 straight insertions and 1 angulated insertions).

A total of 46 insertions were included in the statistical analysis. Overall, the average targeting error of all insertions was 9.1±2.7 mm (mean±SD). However, the result showed a systematic error in both right-left (horizontal) and anterior-posterior (vertical) directions due to the calibration of encoders, and fixation of the Smart Template to the table. As a result, the measurements along the anterior-posterior and right-left axis were not normally distributed around the target as one should expect preventing us from estimating the influence of anatomic structures on the needle deviations. To compensate for this bias, we performed an *a-posteriori* bias correction by subtracting the bias from the target position along each axis independently. Considering a target located at $(p_R,\ p_A,\ p_S)$, where $p_R,\ p_A$ and p_S are the RAS coordinates. The target location after the bias correction is then given by $(p_R - p_{bias-R},\ p_A - p_{bias-A},\ p_S)$, where p_{bias-R} and p_{bias-A} are the bias along the right-left axis (R) and the anterior-posterior axis (A), respectively.

The bias had to be calculated separately for each animal model (i.e., three different bias values for each axis), because both registration and encoder calibration were performed for each animal model. The bias was defined as the value required to centralize the error along the right-left (R) and the anterior-posterior (A) axes separately. The biases along axis R were −4.53 mm, 4.21 mm, 6.19 mm for the first, second and third animal models, respectively, while the biases on axis A were −4.47 mm, −6.15 mm, −7.31 mm, respectively. It is important to highlitght that the bias correction was only performed to correct the errors associated with the animal experiments.

For experiment 1, 15 pairs of straight and angulated insertions were performed on 15 targets (30 insertions). Among these targets, nine were not behind the bulbospongiosus, and thus the angulated insertion was selected under the proposed strategy. The targeting errors with straight insertion only, angulated only and with the path selection strategy were 9.2±3.3 mm, 8.6±2.2 mm and 7.9±1.6 mm respectively, before the bias correction. The Shapiro-Wilk tests provided no evidence that the absolute targeting errors were not normally distributed (p=0.78, p=0.92 and p=0.94, respectively), and the paired t-test did not show statistically significant difference between the straight only and the angulated only (p=0.60), and between the straight only and the path selection strategy (p=0.21). On the other hand, after the bias correction, the Shapiro-Wilk tests provided evidence that the absolute targeting errors were not normally distributed (p=0.024, p=0.047 and p=0.029, respectively), and the median values and the interquartile ranges were (median [IQR]): 3.9 mm [2.4–5.0], 2.8 mm

[1.8–3.9] and 2.4 mm [1.3–3.7] for the straight only, angulated only and using the selection strategy, respectively. The logarithmic transformation was used to normalize the three datasets for hypothesis testing. The paired t-test did not show statistically significant difference between the straight only and the angulated only (p=0.39), but a statistically significant difference was observed when comparing the corrected targeting errors obtained with the straight only approach and with the proposed path selection strategy (p=0.041). One representative example of an angulated insertion outperforming the straight insertion is shown in Figure 8. The in-plane targeting error for all insertions is presented in Figure 9 with their 95% confidence ellipsoid.

For Experiment 2, additional straight and angulated insertions were repeated in four of the 15 targets used in Experiment 1 (8 extra insertions), using the same insertion paths. The targeting error with single straight insertion before the systematic error correction was 8.3±1.2 mm, and it was reduced to 7.2±2.7 mm with repeated straight insertions. After the bias correction, the median targeting error was 3.7 mm [2.7–6.5] and it was reduced to 2.2 mm [1.5–4.9] with repeated straight insertions. Although the mean error was reduced, there was no statistically significant difference between the single and repeated insertions (p=0.39). The median targeting error with the path selection strategy was 2.7 mm [1.8–3.4] for the same four targets after the bias correction, though it was not statistically significantly smaller than the repeated insertion approach (p=0.50). The results of the experiments using the path selection strategy are summarized in Table 1. Experiment 3 analyzed straight and vertically angulated insertions in 4 targets (8 insertions), and showed that the vertical angulation was successfully performed. The targeting errors with the straight and vertically angulated insertions in these targets were 6.9±2.9 mm and 6.2±2.4 mm (p=0.37), respectively and after the bias correction.

IV. DISCUSSION

The study presented an analysis of different insertion paths using a new 4-DoF needle-guide Smart Template that allows angulating the needle insertion path to a given target. It demonstrated that the additional DoF allowed selecting an alternative path to mitigate needle deviation and improved needle placement accuracy. To the best of our knowledge, this was the first study to quantitatively show the benefit of angulated needle insertion to the targeting accuracy *in vivo*. Although a few other studies have also used angulated insertions in transperineal prostate biopsy, the use of the subject's anatomy to improve targeting accuracy had not been explored.

The benchtop evaluation performed in the laboratory demonstrated that the Smart Template could position the needle guide with a translational and angular error of less than 1 mm and 0.5°, respectively. Considering a typical insertion depth for transperineal biopsy (80 mm on average in our previous study[18]), the angulation error of 0.5° is equivalent to an error of 0.7 mm at the needle tip. These results are consistent with the free-space insertion analysis, which had an overall average targeting error of 1.3 mm. It is worth mentioning that the targeting error in free-space has two main sources: 1) manually adjusting the insertion depth, and 2) inaccuracies related to the mechanical design. There are a few factors in the mechanical design that affected the positioning accuracy. First, the play at the two spherical

joints that orients the needles guide contributes to the angulation error. Second, the horizontal and vertical translation accuracies were limited by the precision of the timing belt mechanism. On the contrary, the piezo motors, which adjust the orientation of the needle, are directly placed on the angulation stage, providing a well-defined motion. However, the piezomotors are a friction-based actuator that relays on the clamping force. Initially, the angulation stages were fabricated with a Ceramic-Like material (Ceramic-Like White, Protolabs, Maple Plain, MN, USA), which was not rigid enough and would flex under the load in extreme circumstances, resulting in misalignment of the optical encoder. In order to improve the reliability of the system, after the *in-vivo* animal experiments, we changed the material of the stages to titanium (Ti-6Al-4V, Grade 5 per ASTM B265. In addition, by switching to titanium, we eliminate the flexing of the stages, and significantly increase the output force of the piezo motor and provides a more reliable calibration. While there are few published clinical studies showing the impact of needle placement accuracy on the diagnostic accuracy, the simulation study by Robertson *et al* shows that 2-core and 3-core targeted biopsies outperform 12-core systematic biopsy in terms of cancer sensitivity, when the targeting error is less than 6 mm.[6] The same study shows that the sensitivity of single-core targeted biopsy can be significantly improved by reducing the targeting error. The movement accuracy achieved in our evaluation allows us to assume that the performance of the Smart Template is sufficient for targeted biopsy as long as needle deviation is minimal.

In the *in-vivo* study, Experiment 1 demonstrated that the newly developed angulation capability and the path selection strategy improved the targeting accuracy. The result shows that the proposed angulation strategy outperformed the conventional straight insertion with the median targeting error being reduced from 3.9 mm to 2.4 mm after the bias correction. The bias correction was used to eliminate the systematic errors resulting from the experimental setup with the animal models. It is worth note that even before the bias correction, the path selection strategy resulted in a lower average targeting error but without statistical significance. Although the bias correction is an offset adjustment on the target location, the correction was performed for each axis separately and the statistical analysis was performed in the in-plane targeting error, which resulted in a different p-value before and after the bias correction. After correcting for the systematic errors, the median targeting error with the straight insertion (3.9 mm) became consistent with our previous clinical study using the original Smart Template (5.39 mm).[17] Anyhow, it is not our claim that the targeting errors after the bias correction represent the performance of the device *in-vivo*. However, our finding that the proposed strategy resulted in the reduced error should not be affected by the bias correction. Therefore, our study showed new evidence that this strategy can potentially reduce needle deviation and hence improve the needle placement accuracy. The strategy used in this study was based on our previous clinical study,[18] where we found that the needle trajectories that crossed the bulbospongiosus resulted in smaller targeting errors. While this finding has not been fully understood and needs further validation, one hypothesis is that the needle trajectory is affected by the presence of the pelvic diaphragm (Figure 5). Since the pelvic diaphragm has a canal around the urethra (or the base of the bulbospongiosus), it is likely that many of the trajectories that crossed the bulbospongiosus passed through the canal and were not affected by the pelvic diaphragm. Nevertheless, the new mechanism allowed the needle to avoid certain anatomical structures and helped to

improve the needle placement accuracy in vivo. In Experiment 2, we attempted to compare the effect of the proposed angulation strategy with the common clinical practice of repeated insertion. The result shows a trend that the repeated insertion improved the targeting accuracy (3.7 mm [2.7 – 6.5] vs 2.2 mm [1.5–4.9]), which agrees with the simulation study presented by Robertson et al.6 Our result also suggests that the proposed strategy resulted in a similar result compared to the repeated insertion with a small reduction of the range (2.7 mm [1.8–3.4] vs 2.2 mm [1.5–4.9]). However, both findings are not statistically significant probably due to the lack of statistical power and large standard deviation of straight insertions. On the other hand, Experiment 3 resulted in similar targeting errors between the straight and the vertically angulated insertions. This result was expected because Experiment 3 was performed to demonstrate the ability to angulate the needle insertion vertically and did not use the path selection strategy as in Experiments 1 and 2. Although these results suggest that a proper insertion path selection can reduce the targeting error, the difference between the swine and human anatomies has to be considered when analyzing the values of the targeting errors, and further evaluations in clinical trials must be performed.

It is worth mentioning that our analysis used the in-plane targeting error to evaluate the accuracy of the needle trajectories, which means that the error along the superior-inferior axis was not considered. The rationale for using such a metric is that when firing the biopsy needle, the inner needle stylet is pushed 20 mm forward to collect the tissue sample in a 17 mm groove. In our experiments. the average targeting error on the superior-inferior axis of all insertions was 11.0 mm without any bias correction, which is within the 17.0 mm range of the tissue sample collected by the biopsy needle. Furthermore, there might be a concern over damaging other anatomic structures, such as the bladder wall, when the needle insertion is performed manually. In clinical practice, if the target is close to any sensitive structure, the physician carefully inserts the needle and uses the confirmation images to assess the needle tip position along the superior-inferior axis iteratively. The physician can then manually adjust the insertion depth by pulling or pushing the needle a few millimeters before firing the biopsy gun. Another concern is the excessive number of insertions, which may affect the needle path and the target location. Repeated insertions may cause an extraprostatic hematoma, a known complication for prostate biopsy, and can lead to the dislocation of the prostate gland due to the pressure, hence affecting the needle path. During our experiments, we performed an MRI scan after each insertion and confirmed that there was no hematoma. In addition, to avoid a change of the mechanical property of the tissue due to the needle injury, we spread the target locations to minimize repetitive insertions in the same area.

The results indicate the advantage of using a patient-specific anatomy-based needle path selection, but our study has other limitations. First, the Smart Template could not be secured to the patient table in the same way as the human study probably leading to additional targeting error. Although a custom-made table was developed to secure both the patient and the Smart Template for our previous clinical study,[19] it could not be used with the animal model due to the differences in the size and shape of the subject and the model of the MRI scanner. Second, in its current version, the Smart Template caused an SNR decrease on the MR images, which might undermine the localization of the suspected lesion in a clinical case. However, for the animal experiments performed in this study, the decrease in the SNR did not impair the needle trajectory analysis. Even though the device does not require to be

powered on during the imaging scans, improvements on the shielding, grounding, and MRI-compatibility will be performed to minimize the SNR decrease. Finally, the difference between the swine and the human anatomy made it challenging to place the Smart Template and the MR receiver coil in the same way as in the human study. This difference affected the calibration image quality, which resulted in less accurate calibration and contributed to the systematic error encounter in the animal experiments. Considering that most of the bias observed in this study was directly related to the limitations of the experimental setup in the animal experiments and considering the system's ongoing improvements, the bias correction performed in Section III.B will likely not be necessary for future tests and clinical trials.

In this study, the Smart Template was used as a tool to explore our working hypothesis of the impact of an anatomy-based path selection strategy in the targeting accuracy. Future work will focus on the improvements in the system necessary for clinical trials. Besides, a path planner using patient-specific information is being implemented in 3D Slicer to automatically suggest the best insertion angle given the patient's anatomy and target location.

IV. CONCLUSION

We presented an *in-vivo* analysis comparing straight and angulated insertions using a new four DoF needle-guide manipulator called Smart Template that allows guiding a biopsy needle to a target from different angles. The results show that the new capability to angulate the needle path allows avoiding the anatomical structure that is likely to deviate the needle, and improve the targeting accuracy. The study highlights the importance of a personalized procedure plan, where the patient-specific anatomy is taken into account to achieve a better clinical outcome in transperineal prostate biopsies.

ACKNOWLEDGEMENT

The study was funded in part by the National Institutes of Health (4R44CA224853, R01EB020667, R01CA235134, P41EB028741). The content of the material is solely the responsibility of the authors and does not necessarily represent the official views of these agencies.

The authors thank Lori Foley for her dedication and excellent support during the *in-vivo* animal experiments.

CONFLICTS OF INTEREST

JT received grant support through the institution provided by Siemens Healthineers for a separate study. His interest was reviewed and is managed by Brigham and Women's Hospital and Partners HealthCare in accordance with their conflict of interest policies. JG, NI, and JP are employees of Physical Science Inc.

DATA AVAILABILITY STATEMENT

The data that support the findings of this study are available on request from the corresponding author, JT.

REFERENCES

1. Siegel RL, Miller KD, Jemal A. Cancer statistics, 2020. CA Cancer J Clin. 2020;70(1):7–30. doi:10.3322/caac.21590 [PubMed: 31912902]

2. Panebianco V, Barchetti F, Sciarra A, et al. Multiparametric magnetic resonance imaging vs. standard care in men being evaluated for prostate cancer: A randomized study. Urol Oncol Semin Orig Investig. 2015;33(1):17.e1–17.e7. doi:10.1016/j.urolonc.2014.09.013

3. Barentsz JO, Weinreb JC, Verma S, et al. Synopsis of the PI-RADS v2 Guidelines for Multiparametric Prostate Magnetic Resonance Imaging and Recommendations for Use. Eur Urol. 2016;69(1):41–49. doi:10.1016/j.eururo.2015.08.038 [PubMed: 26361169]

4. De Rooij M, Hamoen EHJ, Fütterer JJ, Barentsz JO, Rovers MM. Accuracy of multiparametric MRI for prostate cancer detection: A meta-analysis. Am J Roentgenol. 2014;202(2):343–351. doi:10.2214/AJR.13.11046 [PubMed: 24450675]

5. Kasivisvanathan V, Rannikko AS, Borghi M, et al. MRI-targeted or standard biopsy for prostate-cancer diagnosis. N Engl J Med. 2018;378(19):1767–1777. doi:10.1056/NEJMoa1801993 [PubMed: 29552975]

6. Robertson NL, Hu Y, Ahmed HU, Freeman A, Barratt D, Emberton M. Prostate cancer risk inflation as a consequence of image-targeted biopsy of the prostate: A computer simulation study. Eur Urol. 2014;65(3):628–634. doi:10.1016/j.eururo.2012.12.057 [PubMed: 23312572]

7. Stoianovici D, Kim C, Srimathveeravalli G, et al. MRI-Safe Robot for Endorectal Prostate Biopsy. IEEE/ASME Trans Mechatronics. 2014;19(4):1289–1299. doi:10.1109/TMECH.2013.2279775

8. Schouten MG, Bomers JGR, Yakar D, et al. Evaluation of a robotic technique for transrectal MRI-guided prostate biopsies. Eur Radiol. 2012;22(2):476–483. doi:10.1007/s00330-011-2259-3 [PubMed: 21956697]

9. Krieger A, Song S, Cho NB, et al. Development and Evaluation of an Actuated MRI-Compatible Robotic System for MRI-Guided Prostate Intervention. IEEE/ASME Trans Mechatronics. 2013;18(1):273–284. doi:10.1109/TMECH.2011.2163523

10. Goldenberg AA, Trachtenberg J, Yi Y, et al. Robot-assisted MRI-guided prostatic interventions. Robotica. 2010;28(2):215–234. doi:DOI: 10.1017/S026357470999066X

11. van den Bosch MR, Moman MR, van Vulpen M, et al. MRI-guided robotic system for transperineal prostate interventions: proof of principle. Phys Med Biol. 2010;55(5):N133–40. doi:10.1088/0031-9155/55/5/N02 [PubMed: 20145293]

12. Su H, Shang W, Cole G, et al. Piezoelectrically Actuated Robotic System for MRI-Guided Prostate Percutaneous Therapy. IEEE/ASME Trans Mechatronics. 2015;20(4):1920–1932. [PubMed: 26412962]

13. Moreira P, van de Steeg G, Krabben T, et al. The MIRIAM Robot: A Novel Robotic System for MR-Guided Needle Insertion in the Prostate. J Med Robot Res. 2016;02(04):1750006. doi:10.1142/S2424905X17500064

14. Zangos S, Melzer A, Eichler K, et al. MR-compatible assistance system for biopsy in a high-field-strength system: Initial results in patients with suspicious prostate lesions. Radiology. 2011;259(3):903–910. doi:10.1148/radiol.11101559 [PubMed: 21364080]

15. Zangos S, Eichler K, Engelmann K, et al. MR-guided transgluteal biopsies with an open low-field system in patients with clinically suspected prostate cancer: Technique and preliminary results. Eur Radiol. 2005;15(1):174–182. doi:10.1007/s00330-004-2458-2 [PubMed: 15351902]

16. Stoianovici D, Kim C, Petrisor D, et al. MR Safe Robot, FDA Clearance, Safety and Feasibility of Prostate Biopsy Clinical Trial. IEEE/ASME Trans Mechatronics. 2017;22(1):115–126. [PubMed: 28867930]

17. Tilak G, Tuncali K, Song S-E, et al. 3T MR-guided in-bore transperineal prostate biopsy: A comparison of robotic and manual needle-guidance templates. J Magn Reson Imaging. 2015;42(1):63–71. doi:10.1002/jmri.24770 [PubMed: 25263213]

18. Moreira P, Patel N, Wartenberg M, et al. Evaluation of robot-assisted MRI-guided prostate biopsy: Needle path analysis during clinical trials. Phys Med Biol. 2018;63(20). doi:10.1088/1361-6560/aae214

19. Song S, Tokuda J, Tuncali K, Tempany CM, Zhang E, Hata N. Development and Preliminary Evaluation of a Motorized Needle Guide Template for MRI-Guided Targeted Prostate Biopsy. IEEE Trans Biomed Eng. 2013;60(11):3019–3027. doi:10.1109/TBME.2013.2240301 [PubMed: 23335658]

20. Penzkofer T, Tuncali K, Fedorov A, et al. Transperineal in-bore 3-T MR imaging-guided prostate biopsy: A prospective clinical observational study. Radiology. 2015;274(1):170–180. doi:10.1148/radiol.14140221 [PubMed: 25222067]

21. Tokuda J, Fischer GS, DiMaio SP, et al. Integrated navigation and control software system for MRI-guided robotic prostate interventions. Comput Med Imaging Graph. 2010;34(1):3–8. doi:10.1016/j.compmedimag.2009.07.004 [PubMed: 19699057]

22. Tokuda J, Fischer GS, Papademetris X, et al. OpenIGTLink: an open network protocol for image-guided therapy environment. Int J Med Robot Comput Assist Surg. 2009;5(4):423–434. doi:10.1002/rcs.274

23. Frank T, Krieger A, Leonard S, Patel NA, Tokuda J. ROS-IGTL-Bridge: an open network interface for image-guided therapy using the ROS environment. Int J Comput Assist Radiol Surg. 2017;12(8):1451–1460. doi:10.1007/s11548-017-1618-1 [PubMed: 28567563]

24. Fedorov A, Beichel R, Kalpathy-Cramer J, et al. 3D Slicer as an image computing platform for the Quantitative Imaging Network. Magn Reson Imaging. 2012;30(9):1323–1341. doi:10.1016/j.mri.2012.05.001 [PubMed: 22770690]

25. Abayazid M, Roesthuis RJ, Reilink R, Misra S. Integrating deflection models and image feedback for real-time flexible needle steering. IEEE Trans Robot. 2013;29(2):542–553. doi:10.1109/TRO.2012.2230991

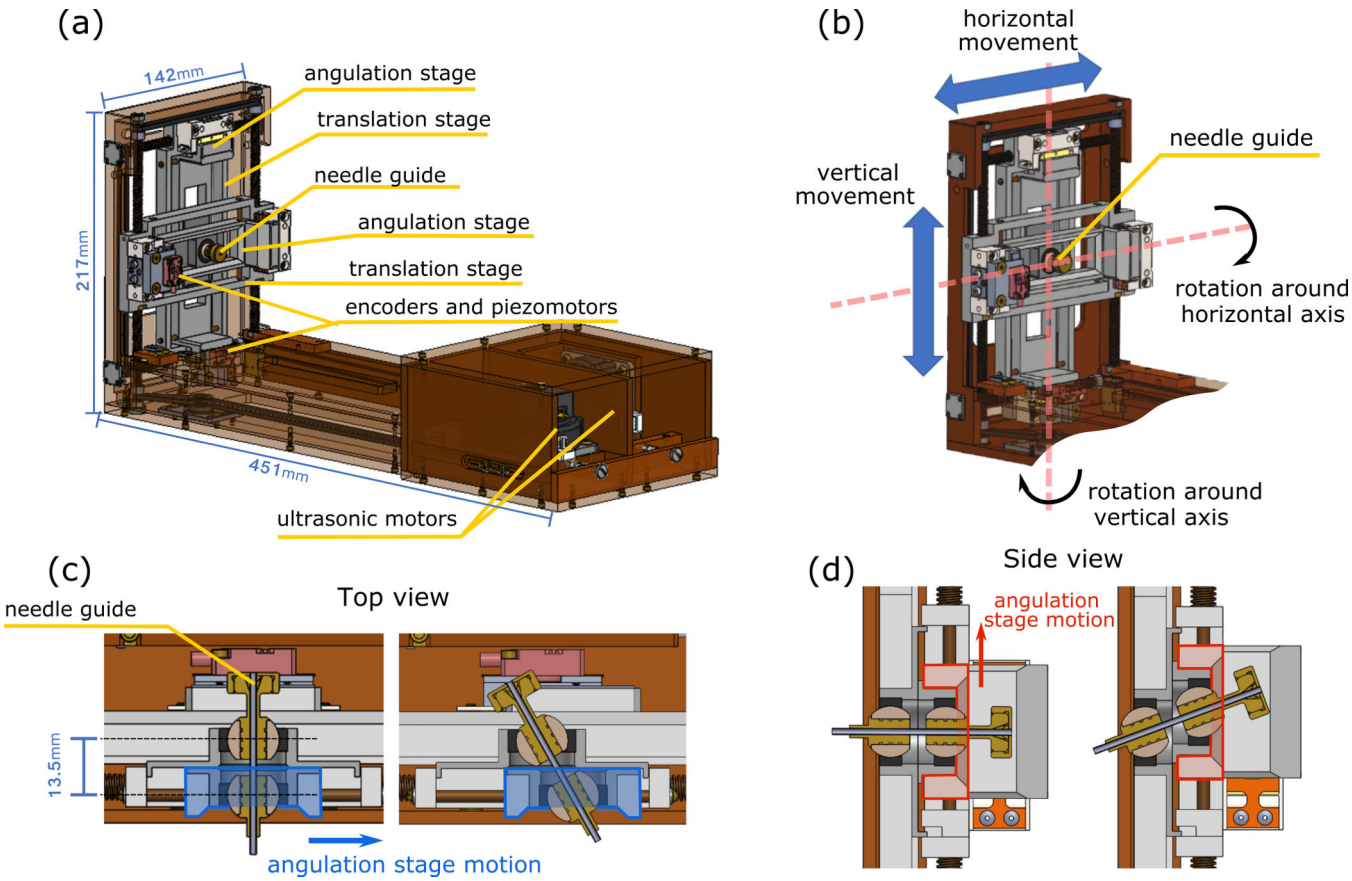

Figure 1:

(a) The main components of the new Smart Template. The ultrasonic motors are mounted on the back of the device, while the piezoelectric motors are directly mounted on the angulation stages. (b) The Smart Template was designed to allow for two-degree-of-freedom (DoF) actuation of the needle guider in the RA-directions and two independent tilting DoFs to angulate the needle-guide. Figures (c) and (d) shows the horizontal and vertical angulation stages moving within the translation stages to provide the needle guide angulation, respectively.

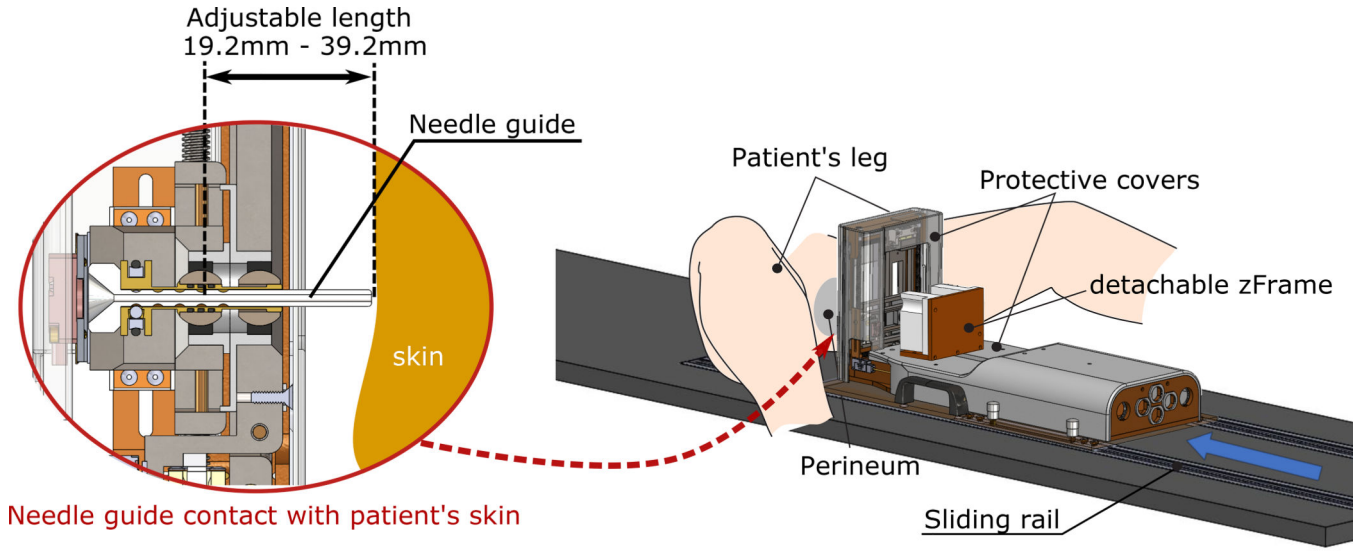

Figure 2:

Smart Template installation. The physician places the device on a custom made patient table and adjust the device against the patient perineum as close as possible. The needle guide is extended until soft contact is made with the patient skin.

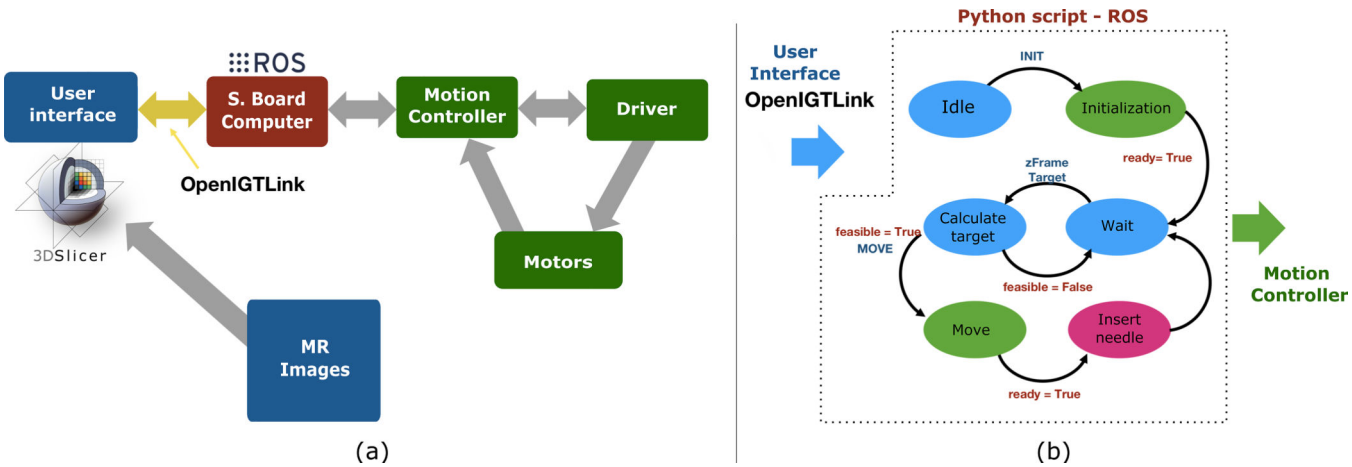

Figure 3:

(a) The control architecture of the Smart Template is composed of the user interface and the low-level controller connected via single-board computer (SBC) with Robot Operating System (ROS). (b) The communication between the user interface and the controller is managed by a python script on ROS, which receives command messages from the user interface using OpenIGTLink and send the appropriate commands to the motion controller.

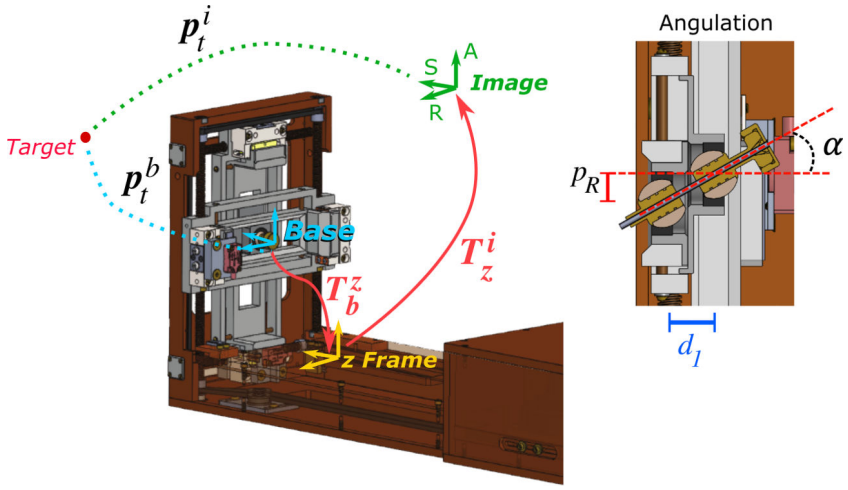

Figure 4:

Coordinate frames for registration of device to MRI image space and to translate the target location from the image reference frame to the device base frame (i.e., the homing position). On the left, the angulation stage motion (p_R) provides a tilting angle α considering the distance d_1 between the two ball joints.

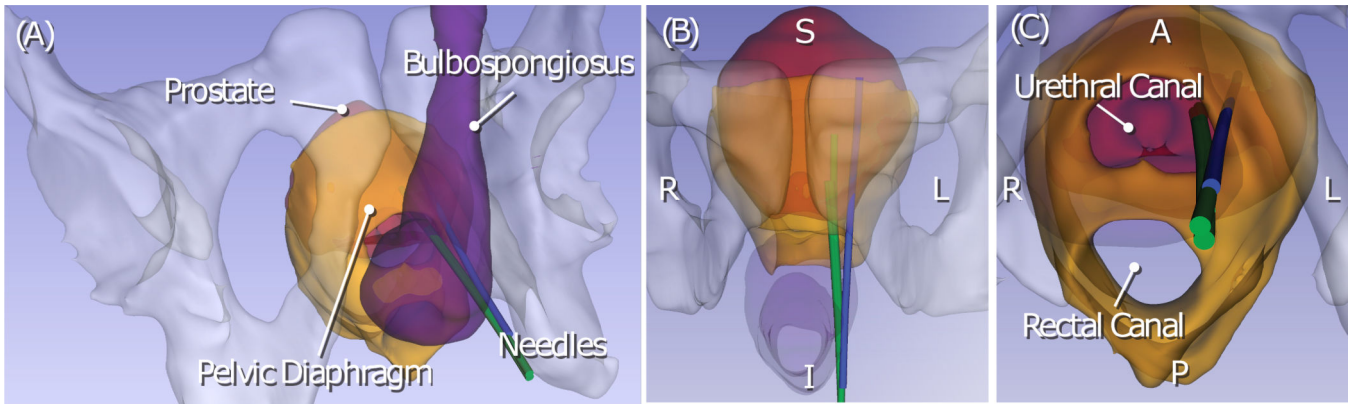

Figure 5:

Trajectories of the biopsy needle during MRI-guided transperineal prostate biopsy were reconstructed from intraprocedural MRI and rendered in three different view angles (A-C). The renderings also show relevant anatomical structures including the pelvis, the prostate, the pelvic diaphragm, and the bulbospongiosus. Although all three trajectories were aimed at the same target with the same needle guide position, the insertion trajectory that penetrates the pelvic diaphragm (blue trajectory) was deviated laterally from the other two trajectories. The other two trajectories (green trajectory) pass through the urethral canal.

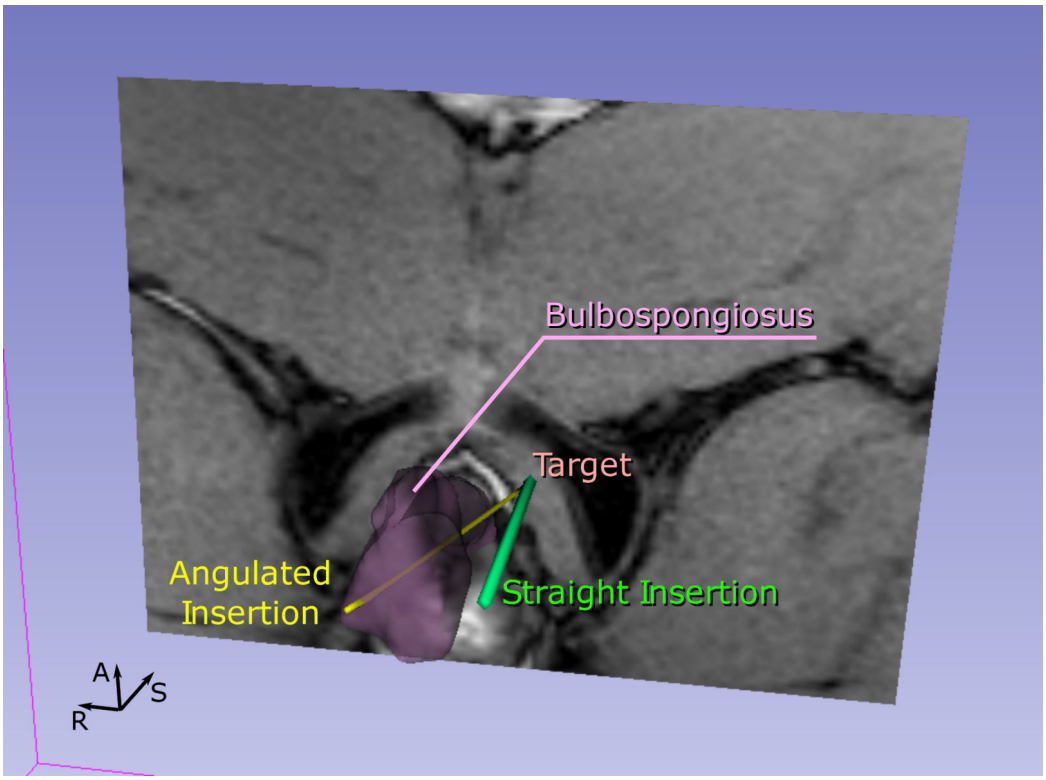

Figure 6:
The planned insertions for a given target. For each target, we performed a conventional insertion parallel to the static field (straight insertion) and an insertion titled from the static field. However, the proposed path selection strategy considers the straight insertion for targets within the central targeting zone (i.e. behind the bulbospongiosus) and the angulated insertion crossing the bulbospongiosus for targets outside this zone.

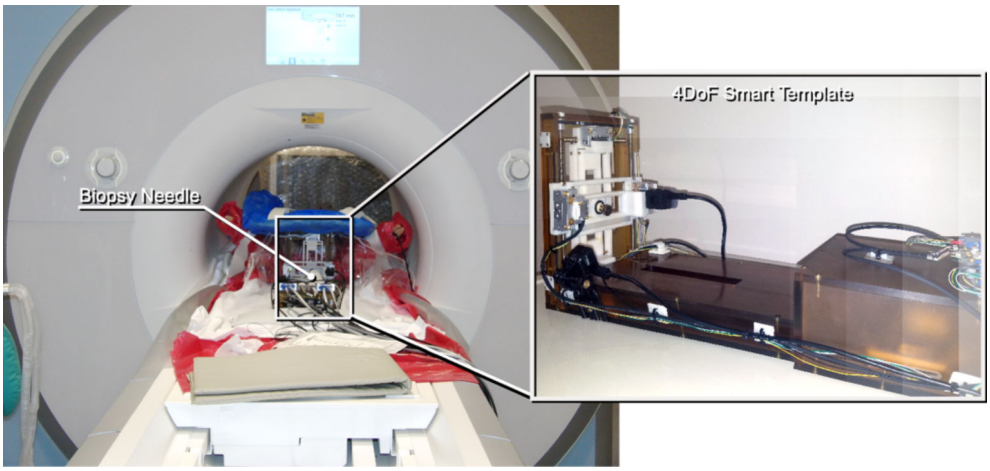

Figure 7:
The prototype 4-DoF Smart Template was placed at the perineum of the subject in the lithotomy position in the 3-Tesla MRI scanner. The subject stayed at the isocenter throughout the procedure.

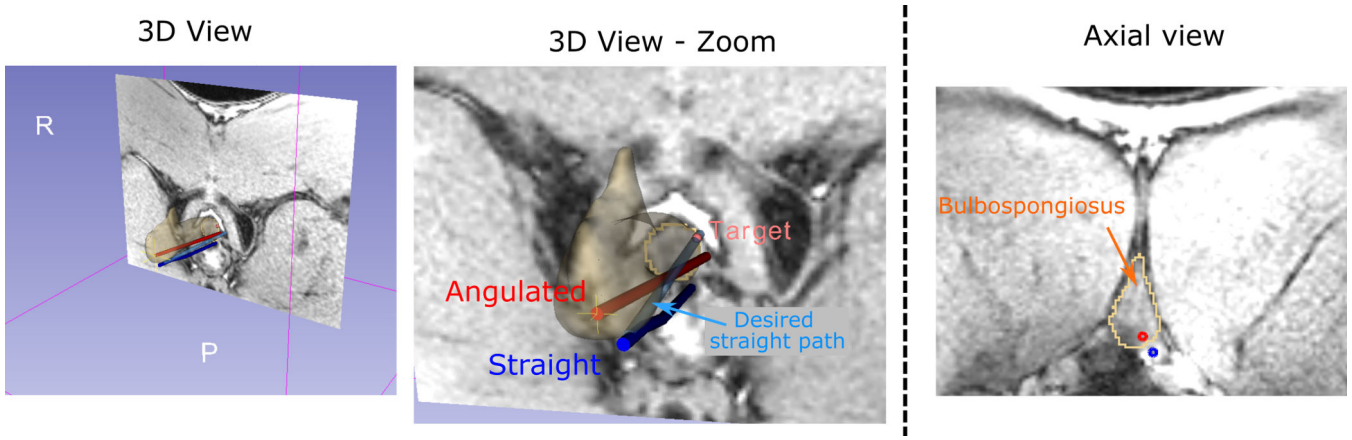

Figure 8:

A representative case of an angulated insertion crossing the bulbospongiosus outperforming the straight insertion. In this case, while the straight trajectory presented a downward (posterior) deviation probably due to the interaction with the pelvic diaphragm, the angulated trajectory crossed the bulbospongiosus, resulting a reduced targeting error.

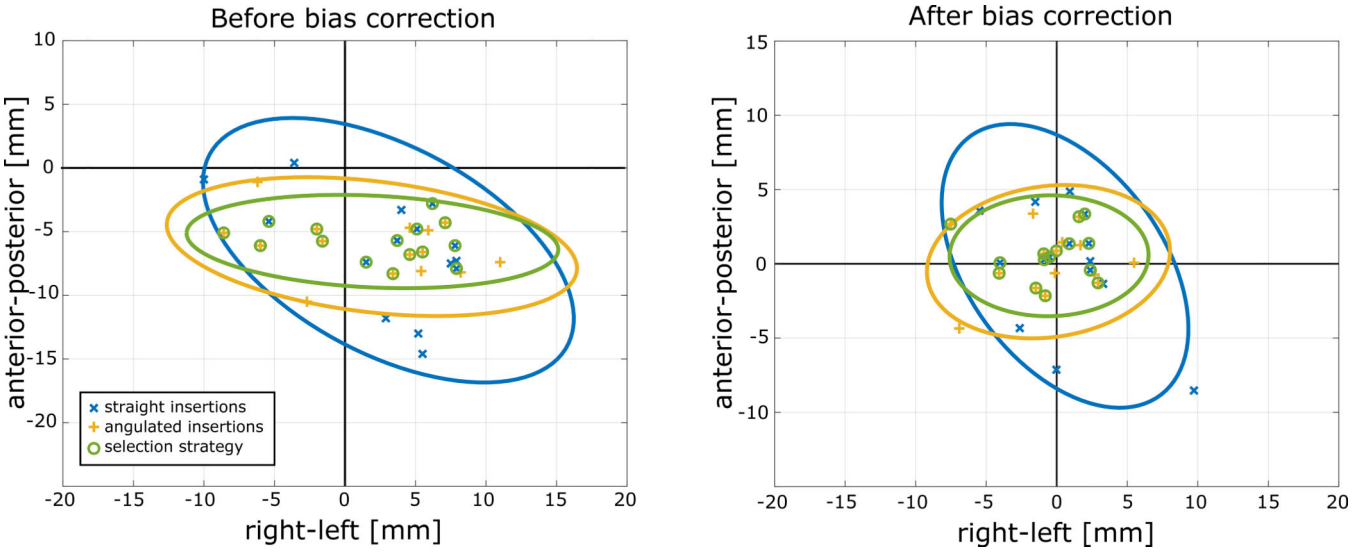

Figure 9:

Targeting errors on the RA-plane (right-left/anterior-posterior) and their 95% confidence ellipsoid. The image on the left shows the targeting error before the bias correction of the straight insertions (blue), angulated insertion (yellow), and using the path selection strategy (green). The image on the right shows the same errors after the bias correction. It is possible to observe that the 95% ellipsoid area using the path selection strategy is significantly smaller than using the standard straight only approach both before and after the bias correction. The bias observed in this study was directly related to the setup in the animal experiments, and therefore the correction will not be necessary for the future clinical trials.

Table 1.

Comparison of the average targeting error achieved in Experiments 1 and 2. In Experiment 1, we compared only straight insertions, only angulated insertions, and the proposed path selection strategy. In Experiment 2, we compared a single straight insertion, repeated straight insertions, and using the proposed path selection strategy.

		Before the bias correction				After the bias correction		
Exp. 1		Straight	Angulated	Strategy		Straight	Angulated	Strategy
	Mean ±SD	9.2±3.3 mm	8.6±2.2 mm	7.9±1.6 mm	*Median [IQR]*	3.9 mm [2.4 – 5.0]	2.8 mm [1.8–3.9]	2.4 mm [1.3–3.7]
					*LOG±SD**	1.19±0.74	0.96.±0.72	0.81±0.66
Exp. 2		Straight	Repeated	Strategy		Straight	Repeated	Strategy
	Mean ±SD	8.3±1.2 mm	7.2±2.7 mm	7.8±1.7 mm	*Median [IQR]*	3.7 mm [2.7 – 6.5]	2.2 mm [1.5–4.9]	2.7 mm [1.8–3.4]
					*LOG±SD**	1.31±0.84	0.97±1.09	0.82±0.66

LOG±SD is the mean value and the standard deviation on the natural log scale.